Ceramics International 49 (2023) 1800–1810

Contents lists available at ScienceDirect

Ceramics International

journal homepage: www.elsevier.com/locate/ceramint

Enhanced electrochemical performance of hybrid composite microstructure of $CuCo_2O_4$ microflowers-NiO nanosheets on 3D Ni foam as positive electrode for stable hybrid supercapacitors

Nagesh Maile [a], Surendra Shinde [b], Youngsu Lim [a], Bolam Kim [a], Ahsan Abdul Ghani [a], Khurram Tahir [a], Muzammil Hussain [a], Jiseon Jang [c], Dae Sung Lee [a,*]

[a] *Department of Environmental Engineering, Kyungpook National University, 80 Daehak-ro, Buk-gu, Daegu, 41566, Republic of Korea*
[b] *Department of Biological and Environmental Science, College of Life Science and Biotechnology, Dongguk University, 32 Dongguk-ro, Biomedical Campus, Ilsandong-gu, Siksa-dong, 10326, Goyang-si, Gyeonggi-do, Republic of Korea*
[c] *R&D Institute of Radioactive Wastes, Korea Radioactive Waste Agency, 174 Gajeong-ro, Yuseong-gu, Daejeon, 34129, Republic of Korea*

ARTICLE INFO

Keywords:
Hybrid nanocomposite
$CuCo_2O_4$
NiO
Hybrid supercapacitor
Stability

ABSTRACT

Self-assembled composite porous structures comprising $CuCo_2O_4$ microflowers and NiO hexagonal nanosheets were synthesized on a conducting 3D Ni foam surface [CCO/NO] using a simple hydrothermal method. This unique composite assembly was further characterized and electrochemically evaluated as a binder-free positive electrode for hybrid supercapacitor application. The study showed that the CCO/NO exhibited a maximum areal capacitance of 1444 mF cm^{-2}, significantly higher than the parent $CuCo_2O_4$ and NiO electrodes, with remarkable stability of 88.5% for 10,000 galvanostatic charge-discharge cycles. Key features for the enhanced electrochemical performance of CCO/NO can be related to a lowered diffusion resistance because the hybrid nanocomposite porous assembly generates short diffusion paths for electrolyte ions and more active sites for reversible faradaic transition for charge storage. The hybrid supercapacitor was assembled using activated carbon as a negative electrode and CCO/NO as a positive electrode in alkaline electrolyte, performed at an improved potential of 1.6 V. Device showed a maximum areal capacitance of 122 mF cm^{-2}, a maximum areal energy density of 43 μWh cm^{-2}, and a maximum areal power density of 5.1 mW cm^{-2}. This hybrid supercapacitor showed remarkable cyclic stability up to 98% for 10,000 cycles. This study encourages the development of low-cost, high-performance, durable electrode designs using hybrid composite for next-generation energy storage systems.

1. Introduction

Sustainable energy storage becomes crucial for developing modern technology, such as electric vehicles, miniaturized/portable electronic devices, smart grids, and medical implants, as fossil fuel is depleting and demand for CO_2 reduction is becoming inevitable. Li-ion battery technology has been focused as high energy density storage application [1,2]. Meanwhile, the efficient supercapacitors (SCs) with high energy, power output and extended lifetime have been a vital and supporting to Li-ion battery technology for the sustainable energy storage [3–5]. In SCs, electrostatic interactions or faradaic redox reactions are responsible for the electrochemical energy storage [6,7]. Electrostatic interaction involves numerous rapid kinetic interactions as the charges electrostatically accumulate on the electrode-electrolyte interface, delivering high power density to SCs. However, Faradaic storage involves reversible kinetically faster redox reactions at the electrode-electrolyte interface, producing much higher energy to SCs. Therefore, major studies use state-of-the-art design and development of SC electrodes for simplicity and sustainability by using low-cost, environmentally benign electrochemically active materials that could provide high energy and power densities [3,8–10]. SCs with the most carbon-based 1D, 2D, and 3D material electrodes have been recognized as electric double-layer capacitors (EDLCs), where electrostatic interactions can store the charge. However, SCs with Ni-, Co-, Mn-, and Cu-based metal oxide electrodes have been popular as pseudocapacitors, where faradaic reactions can store the charge [7,11,12]. In both, the electrode electrochemical performance is confined to its thin active surface, so the material overloading at the electrode surface could degrade the SC performance.

---

* Corresponding author.
E-mail address: daesung@knu.ac.kr (D.S. Lee).

https://doi.org/10.1016/j.ceramint.2022.09.143
Received 1 July 2022; Received in revised form 27 August 2022; Accepted 12 September 2022

Therefore during analysis, the quantification of the areal and volumetric electrochemical performance of electrodes has a great deal, along with its gravimetric performance [6,13–15].

Metal oxides, such as MnO_2, NiO, and Co_3O_4, have been considered low-cost, high-performance, widely reported electrode materials for SCs due to their high theoretical capacitance [16–21]. Among them, NiO is an appropriate material because of its low toxicity, minimal environmental impact, high theoretical capacity, and natural abundance [16]. Similarly, bimetallic oxides, such as $NiCo_2O_4$, $CuCo_2O_4$, and $NiMoO_4$, have been widely popular SC electrodes to have improved electrochemical properties ascribed to multiple oxidation states [9,22–25]. Among above bimetallic oxices, $CuCo_2O_4$ is a binary spinal oxide having improved electronic, and electrochemical properties, compared to parent copper and cobalt oxide. Improving Co_3O_4 properties with eco-friendly Cu can be cost-effective [23,26]. Nowadays, 3D hybrid composite with different metal oxide morphologies can synergetically improve performance due to kinetically faster ionic diffusion at enhanced active sites for reversible faradaic reactions. Electrode studies showed a more improved electrochemical performance of hybrid metal oxides than single metal oxides or bimetallic oxides such as $NiO@NiCo_2O_4$ core−shell nanosheet arrays on 3D Ni foam [27], nanoforest of hierarchical $Co_3O_4@NiCo_2O_4$ nanowire arrays [28], hierarchical $Co_3O_4@NiCo_2O_4$ core–shell nanosheets [29], core–shell $CuCo_2O_4@MnO_2$ nanowires on carbon fabrics [30], nanotrees with $CuCo_2O_4$ trunks and NiO branches supported on Ni foam [31], $Cu_{0.56}Co_{2.44}O_4@MnO_2$ core–shell nanoflowers [32], and MnO_2-cladded $CuCo_2O_4$ on Ni foam [33]. Among them, the synergetic effect of $CuCo_2O_4$ with another NiO in the hybrid assembly has been advantageous due to their improved electrical properties [23,26,34]. However, fewer studies have been performed on the $CuCo_2O_4$–NiO hybrids, such as Li-ion batteries [35], glucose sensing [36], and SCs [31,37]. Further studies of $CuCo_2O_4$–NiO hybrid nanocomposite and its electrochemical properties evolution are needed to exploit its possible SC electrode application. The binder-free synthesis of the hybrid electrodes showed a better integration of conducting surfaces with active hybrid materials to boost overall performance [28,29,33]. In-depth study of binder-free designed $CuCo_2O_4$–NiO nanocomposite hybrid can be interesting for developing low-cost high performance SC electrode.

In this study, the composite microstructure comprising $CuCo_2O_4$ microflowers and NiO hexagonal nanosheets was directly grown on a conducting 3D Ni foam surface. This binder-free composite synthesis provided extra redox-active sites for redox transitions and the porous surface, which improved the diffusion of electrolyte ions, boosting the hybrid electrode electrochemical performance. During electrochemical properties evaluation for hybrid SCs, this unique composite microstructure yielded a higher capacitance than parent transition metal oxides nanostructures, such as NiO and $CuCo_2O_4$ and some previously reported transition metal oxides [21,38–40]. This study incorporated X-ray diffraction (XRD), Raman spectroscopy, field emission scanning electron microscopy (FESEM), Transmission electron microscopy (TEM), X-ray photoelectron spectroscopy (XPS), and energy dispersive spectroscopy (EDS) studies for detailed microstructure electrode material study, followed by comparative electrochemical studies as a positive electrode for hybrid SC application.

2. Materials and methods

2.1. Chemicals

The chemicals for the study were of analytical grade; no further purification was needed. Urea [CH_4N_2O], ammonium fluoride [NH_4F], and copper(II)nitrate trihydrate [$Cu(NO_3)_2\cdot 3H_2O$] were purchased from Junsei chemicals Co. Ltd. (Japan). Potassium hydroxide [KOH], cobalt (II) nitrate hexahydrate [$Co(NO_3)_2\cdot 6H_2O$], N-methyl-2-pyrrolidone, and sodium carbonate anhydrous [Na_2CO_3] were purchased from Daejung Chemicals (Republic of Korea). Activated carbon (AC) powder was purchased from Duksan Company (Republic of Korea). Poly(vinylidene fluoride) and carbon black were purchased from Thermo Fisher Scientific (United States of America).

2.2. Preparing NO, CCO, and CCO/NO electrodes

A straightforward hydrothermal method was used for fabricating self-supporting binder-free electrodes. Initially, a piece of battery-grade Ni foam of 1 cm × 2 cm × 0.8 mm was cleaned by ultrasonication in 3 M HCl, deionized water (DI), and ethanol sequentially, to remove the oxide layer from its surface. For NO, a 20 mL precursor solution of 1 M Na_2CO_3 was poured into a 150 mL polytetrafluoroethylene-lined stainless-steel autoclave reactor vessel, and three Ni foam pieces were dipped into this precursor solution. The remaining 130 mL was filled with air to provide sufficient oxygen for the reaction. After tight closure of the reactor vessel, the reaction was conducted at 180 °C for 48 h [17]. After cooling the reactor vessel, the modified Ni foam was cleaned with DI water, dried in an oven at 60 °C, and calcined to 300 °C for 3 h in the furnace to finally obtain an NO electrode. As Ni foam itself participated in the reaction, the amount of material formed on Ni foam before calcination can be estimated using the relation $m = C \times \Delta m$. Where Δm is the Ni-foam's weight difference before and after synthesis and C is the molar ratio of $M_{Ni(OH)_2} / [M_{Ni(OH)_2} - M_{Ni}] = 92.70/34.01$ [41]. Where M is the atomic or molecular weight. The amount of material formed on the Ni-foam is measured as $\sim$2.0 mg cm^{-2}. The amount of weight loss observed after calcination is $\sim$0.8 mg cm^{-2}. So effectively, the mass loading of active material formed on Ni foam for NO is $\sim$1.2 mg cm^{-2}.

In another procedure, 70 mL precursor solution for 1 mM $Cu(NO_3)_2$, 2 mM $Co(NO_3)_2$, 5 mM urea, and 7 mM NH_4F was prepared and poured into a 150 mL polytetrafluoroethylene-lined stainless-steel autoclave reactor vessel. The three pieces of cleaned Ni foam were dipped into the precursor solution. After tight closure of the reactor vessel, the reaction was conducted at 160 °C for 6 h. After cooling the reactor vessel, the modified Ni foam was cleaned with DI water, dried in an oven at 60 °C, and calcined at 300 °C for 3 h to finally obtain the CCO electrode. The amount of active material formed for CCO can be estimated by measuring the weight difference on Ni foam before and after synthesis, which is $\sim$0.6 mg cm^{-2}.

For CCO/NO nanocomposite, the prepared NO electrode was used as the base electrode instead of Ni foam, and a similar synthesis procedure of CCO was followed later to obtain the CCO/NO electrode. The amount of active material formed on Ni foam for CCO/NO is $\sim$1.7 mg cm^{-2}. Fig. 1(a) shows a schematic depiction for synthesizing NO, CCO, and CCO/NO electrodes.

2.3. Preparing the AC electrode

A reported method was used for fabricating an AC electrode [8]. The appropriate amount of AC, carbon black, and polyvinylidene fluoride were mixed with a mass ratio of 80:10:10 and dispersed in 1-methyl-2-pyrrolidinone solvent to form a slurry. This slurry was coated on well-cleaned Ni foam and dried overnight in a vacuum at 80 °C. Finally, the coated Ni foam was pressed with an applied pressure of 10 MPa to obtain the AC electrode.

2.4. Material characterization

XRD studies were conducted using a Panalytical X-ray diffractometer (EMPYREAN, UK) with Cu Kα of 1.54 Å. FESEM studies were conducted using HITACHI SU8230 (Japan). EDS studies were conducted using Oxford Ultim Max100 (UK). Raman studies were conducted using a Raman spectrometer (Renishaw inViareflex spectrometer, Gloucestershire, UK, with a laser line of 532 nm). XPS studies were performed using ThermoFisher -NEXSA, USA. TEM studies were carried out using (TEM) (FE-TEM; Titan G2 ChemiSTEM Cs Probe, Netherlands). The

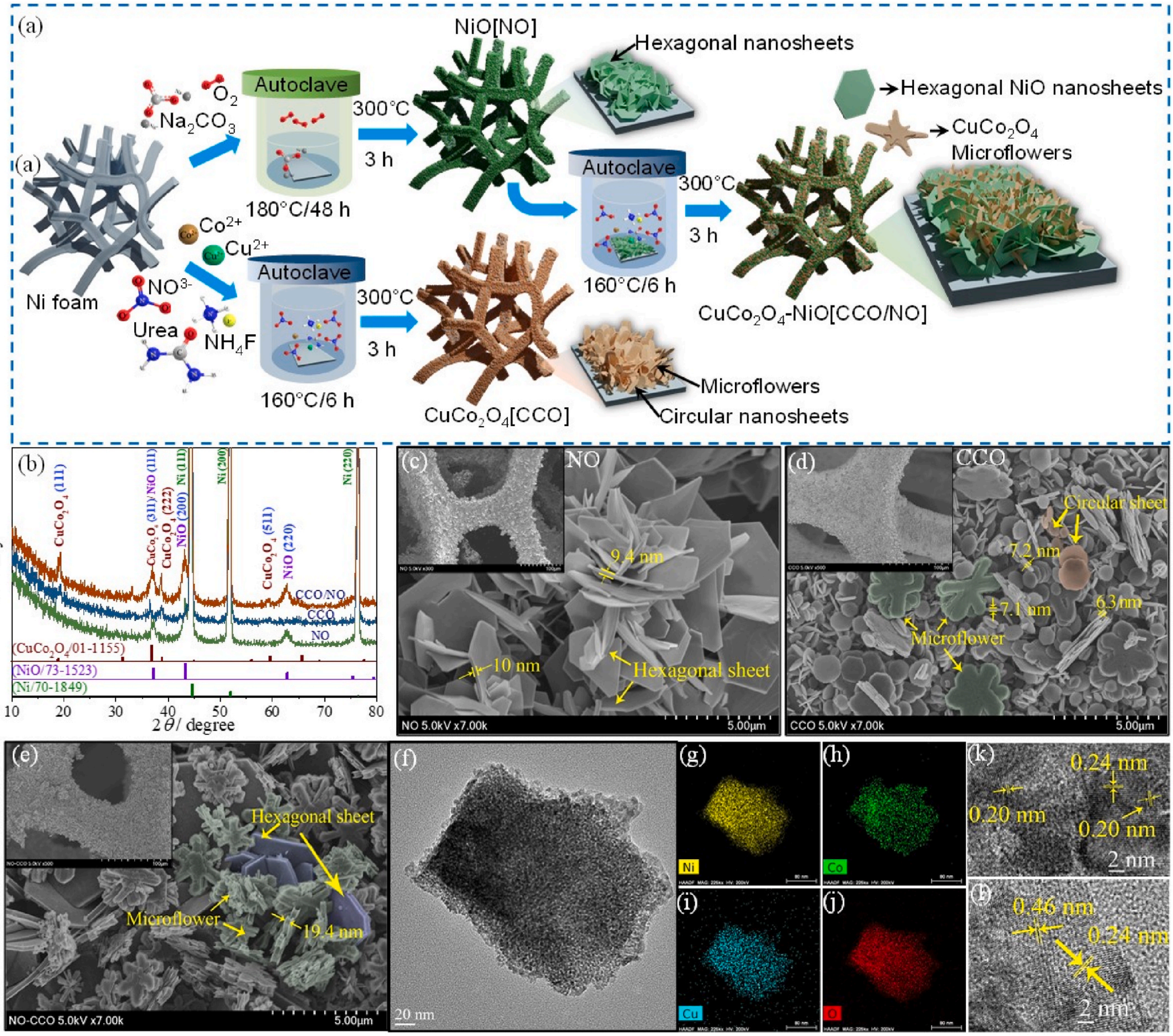

Fig. 1. (a) Schematic for synthesizing NO, CCO, and CCO/NO electrodes. (b) X-ray diffraction (XRD) profiles of NO, CCO, and CCO/NO electrodes. Field emission scanning electron microscopy (FESEM) image of NO(c), CCO(d), and CCO/NO(e) ([Inset: low-resolution FESEM images of modified Ni foam]. TEM image (f) and EDX elemental mapping of Ni-(g), Co-(h), Cu-(i) and O-(j) for CCO/NO. (k–l) HRTEM image of CCO/NO sample.

electrochemical properties of mono electrodes and hybrid SC were studied using the WizEIS 1200 Premium workstation (WizMAC, Republic of Korea). Electrochemical impedance spectroscopy analysis of electrodes was performed using the Ivium CompactStat.h instrument.

2.5. Electrochemical studies

Electrochemical studies were conducted at room temperature. Cyclic voltammetry (CV), galvanostatic charge-discharge (GCD), and electrochemical impedance spectroscopy (EIS) studies of NO, CCO, and CCO/NO electrodes were conducted using the three-electrode system in 2 M KOH electrolyte. The prepared electrodes were used directly as a working electrodes without further processing. Platinum and Hg/HgO (0.098 vs normal hydrogen electrode at 25 °C) were used as counter and reference electrodes, respectively. The following equations can be used to estimate electrochemical parameters [42–44].

Capacitance (C) at different scan rates (ν/V s^{-1}) within a potential window ΔE can be calculated using

$$C = \frac{\int IdE}{2 \times \nu \times \Delta E}\ (\mathrm{F}), \tag{1}$$

where $\int IdE$ is the area under the CV at a given ν.

For nonlinear GCD at different discharge currents (I_{dis}/A), the capacitance can be calculated using

$$C = \frac{2I_{dis}\int Edt}{\Delta E^2}\ (\mathrm{F}), \tag{2}$$

where $\int Edt$ is the area under the discharge GCD curve at given I_{dis}.

For electrodes with a geometrical area (A/cm^{-2}), the areal capacitance (C_A) of the electrode and gravimetric specific capacitance C_{sp} of active material with active mass loading (m) can be calculated as

$$C_A = \frac{C}{A}\ (\mathrm{F\ cm^{-2}}) \tag{3}$$

$$C_{sp} = \frac{C}{m}\left(\mathrm{Fg}^{-1}\right) \tag{4}$$

Similarly, gravimetric capacity Q can be used to estimate the potential independent charge storage performance of the active material by using non-linear GCD curves [17].

$$Q = \frac{I \times \Delta t}{m}\left(C \quad g^{-1}\right) \tag{5}$$

For the hybrid SC, similar formulas can be used for calculating C_A^{SC} of SC from its GCD curves by considering the combined geometrical area of the positive and negative electrode as total the geometrical area. The areal energy (E_A) and power (P_A) densities can be calculated using [5, 45].

$$E_A = \frac{1}{2}\frac{C_A^{SC}(\Delta E)^2}{3600}\left(\mathrm{Whcm}^{-2}\right) \tag{6}$$

and,

$$P_A = \frac{E_A}{\Delta t} \times 3600\left(\mathrm{Wcm}^{-2}\right), \tag{7}$$

Where Δt (s) is the GCD curves discharge time of SC at applied I_{dis}.

3. Results and discussion

3.1. Synthesis, morphology, and characterization

For NO, at a given hydrothermal condition, the Ni foam surface oxidized to form $Ni(OH)_2$ on the Ni surface due to air oxygen that was filled during the closure of the reactor vessel. This formation can be understood by reaction (8) [17,46].

$$2Ni + O_2 + 2H_2O \rightarrow 2\,Ni(OH)_2 \tag{8}$$

Dissolved CO_3^{2-} promotes dissolution and recrystallization during the hydrothermal process [47]. Furthermore, $Ni(OH)_2$ calcination forms NiO on the Ni foam. This formation can be understood by reaction (9) [17].

$$Ni(OH)_2 \rightarrow NiO + H_2O \tag{9}$$

For CCO, thermal hydrolysis of urea generates OH^- ions. Dissolved Cu^{2+} and Co^{2+} ions from the precursor react with generated OH^- at the Ni foam surface and precipitate as $CuCo_2(OH)_6$. In a further step, $CuCo_2(OH)_6$ becomes oxidized during calcination to form $CuCo_2O_4$ on the Ni foam surface. The involved process can be presented by the following reactions [48,49].

$$(CH_2)_6N_4 + 6H_2O \rightarrow 4NH_3 + 6HCHO \tag{10}$$

$$NH_3 + H_2O \rightarrow NH_4^+ + OH^- \tag{11}$$

$$Cu^{2+} + 2Co^{2+} + 6OH^- \rightarrow CuCo_2(OH)_6 \tag{12}$$

$$CuCo_2(OH)_6 + 1/2O_2 \rightarrow CuCo_2O_4 + 3H_2O \tag{13}$$

Similarly, CCO/NO formation can be understood by similar reactions. Fig. S1 shows photos of the as-prepared electrodes before and after calcination. NO appeared grey, and the remaining CCO and CCO/NO appeared dark after calcination. For material confirmation, the XRD of NO, CCO, and CCO/NO was conducted. Fig. 1(b) shows the XRD patterns of NO, CCO, and CCO/NO electrodes. All patterns have a typical sharp peak around 2θ of 44.37°, 51.80°, and 76.35°, associated with metallic Ni foam (JCPDS No. 70–1849) [50]. Apart from metallic Ni, the NO shows diffraction peaks at 2θ of 37.23°, 43.27°, and 62.65°, associated with cubic phase NiO (JCPDS No. 73–1523) [51]. No other impurity peak is observed, confirming NiO formation on the Ni foam surface. Similarly, the CCO shows diffraction peaks at 2θ of 19.23°, 36.51°, 38.78°, and 59.32°, associated with cubic phase spinel $CuCo_2O_4$ (JCPDS No. 01–1155), confirming $CuCo_2O_4$ formation on the Ni foam surface [9]. For CCO/NO, the diffraction peaks observed at 2θ are consistent with cubic NiO and spinel $CuCo_2O_4$, confirming the presence of both material phases on the Ni foam surface. The sharpness of peak intensity shows good crystallinity of formed material. The peak intensities of $CuCo_2O_4$ are lower than NiO, indicating a thin growth of $CuCo_2O_4$ on the NiO surface [52,53].

The surface morphology of the NO, CCO, and CCO/NO was studied using FESEM. Fig. 1(c) shows randomly arranged vertically aligned hexagonal and quasi-hexagonal nanosheets of NiO with a thickness of ~10 nm. These interconnected, standing NiO nanosheets on the Ni surface could provide effective pathways for electron conduction. Voids between nanosheets could be beneficial for electrolyte ion diffusion. This highly porous NiO network was further used as a base electrode surface for the growth of $CuCo_2O_4$ later. Fig. 1(d) shows the randomly distributed mixed microstructure of $CuCo_2O_4$. These microstructures comprise circular-shaped nanosheets and microflower bundles formed by parallel stacked petal-shaped nanosheets. Petal and circular-shaped nanosheets have a thickness of 6–7.5 nm. For CCO/NO, similar microflowers of $CuCo_2O_4$ are randomly formed between NiO hexagonal nanosheet voids (Fig. 1(e)). The microflowers thickness is ~20 nm. A distinct depiction can be observed in high-resolution (HR) FESEM images of CCO/NO (Fig. S2). It shows that the $CuCo_2O_4$ microflowers are formed on the NiO nanosheet surface. TEM image of CCO/NO is shown in Fig. 1(f). EDS mapping image for Ni-(Fig. 1(g)), Co-(Fig. 1(h)), Cu-(Fig. 1(i)), and O- (Fig. 1(j)) elements, showing that fragment of NiO nanosheet is covered with $CuCo_2O_4$ nanosheet, supports the formation of hybrid nanocomposite. HR-TEM image in Fig. 1(k) shows the lattice spacing of 0.20 nm (200) and 0.24 nm (111) of NiO. Similarly, HR-TEM image of Fig. 1(l) shows the lattice spacing of 0.46 nm (111) and 0.24 nm (311) of $CuCo_2O_4$. In further analysis, the EDS of individual electrodes was studied. Fig. 2(a) shows the recorded EDS spectra of NO, CCO, and CCO/NO. The NO EDS spectrum shows elemental peaks of Ni and O, ascribed to have formed NiO on the Ni foam. Similarly, the EDS spectrum of CCO shows elemental peaks of Ni, Cu, Co, and O, ascribed to have formed $CuCo_2O_4$ on the Ni foam. For CCO/NO, the EDS spectrum also shows elemental peaks of Ni, Cu, Co, and O, ascribed to have formed $CuCo_2O_4$ and NiO on the Ni foam.

Moreover, surface chemical properties CCO/NO were studied using Raman and XPS analyses. Fig. 2(b) shows the obtained Raman spectrum of CCO/NO. The two Raman peaks centered around 185 cm^{-1} and 665 cm^{-1} are F_2g and A_1g modes of the spinel $CuCo_2O_4$ phase, respectively [54]. However, the remaining two broad Raman peaks centered around 532 cm^{-1} and 1072 cm^{-1} are of one phonon and two phonon vibrational modes of NiO, respectively [55]. Fig. 2(c) shows the XPS survey spectrum of CCO/NO, showing different peaks associated with a binding energy of Cu 2p, Ni 2p, Co 2p, O 1s, and C 1s orbitals, as depicted in the EDS spectrum of CCO/NO. To see the oxidation states of individual elements, the deconvolution of HR-XPS was conducted. The deconvolution of the Cu 2p HR-XPS spectrum shows the two main characteristics of binding energy peaks at 953.81 eV and 933.86 eV, associated with Cu $2p_{1/2}$ and Cu $2p_{3/2}$, respectively (Fig. 2(d)). The two satellite peaks at 962.45 eV and 941.97 eV confirmed the Cu^{2+} state [3,56]. The deconvolution of the Ni 2p HR-XPS spectrum shows the characteristic of binding energy peaks at 871.75 and 854.08 eV ascribed to Ni $2p_{1/2}$ and Ni $2p_{3/2}$ of Ni^0 from metallic Ni, respectively (Fig. 2(e)). Similarly, the binding energy peaks at 872.98 eV and 855.54 eV, ascribed to Ni $2p_{1/2}$ and Ni $2p_{3/2}$ of Ni^{2+} from NiO, respectively [55,57]. The deconvolution of the Co 2p HR-XPS spectrum shows binding energy peaks at 796.28 eV and 780.89 eV, ascribed to Co $2p_{1/2}$ and Co $2p_{3/2}$ of Co^{2+}, respectively (Fig. 2(f)); similarly, binding energy peaks at 794.71 eV and 779.62 eV, ascribed to Co $2p_{1/2}$ and Co $2p_{3/2}$ of Co^{3+}, respectively. The deconvolution HR-XPS and Raman confirmed that the spinel $CuCo_2O_4$ structure constitutes Cu^{2+}, Co^{2+}, and Co^{3+} oxidation states [8,56]. Moreover, the deconvolution of the O 1s HR-XPS spectrum shows binding peaks at 532.67 eV, 531.09 eV, and 529.51 eV, ascribed to the oxygen from

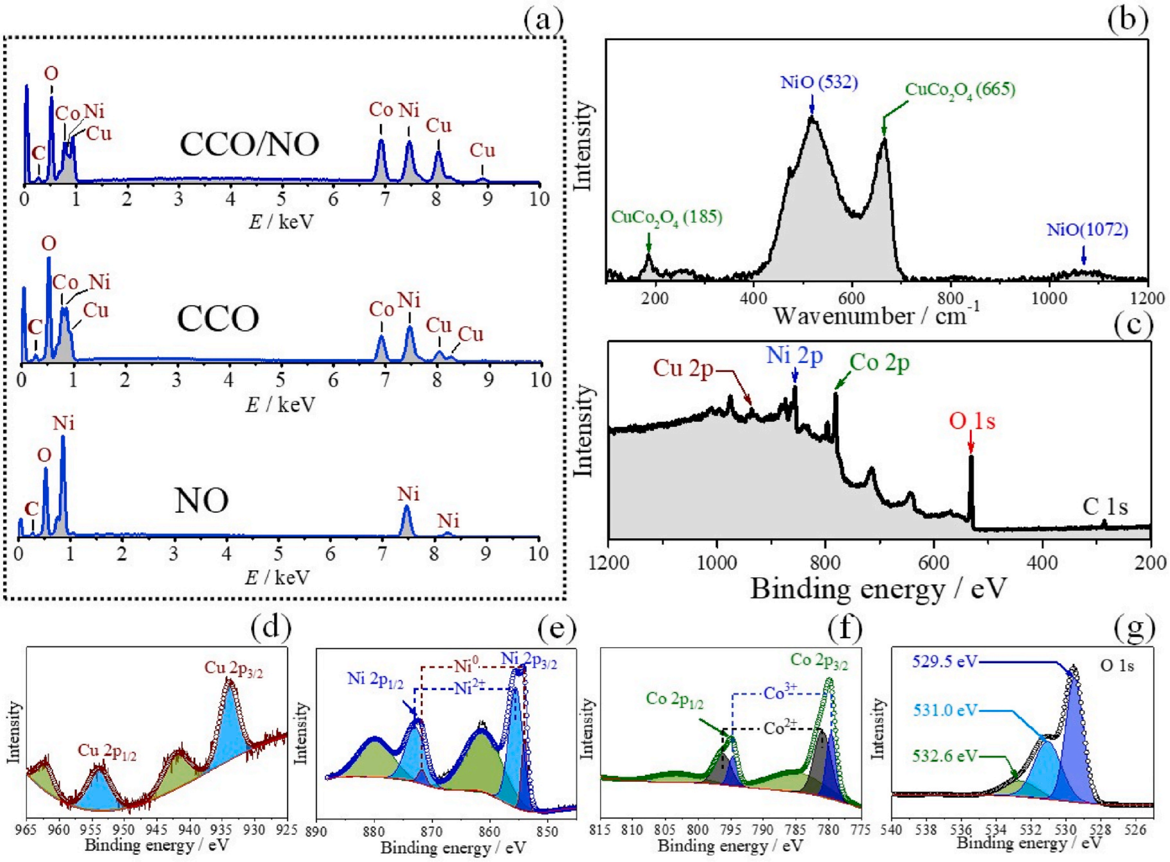

Fig. 2. (a) Energy dispersive spectroscopy (EDS) spectra of NO, CCO, and CCO/NO electrodes. (b) Raman spectrum of CCO/NO. (c) X-ray photoelectron spectroscopy (XPS) survey spectrum of CCO/NO. High-resolution XPS of Cu 2p(d), Ni 2p(e), Co 2p(f), and O 1s(g) orbitals.

adsorbed water at the surface, low coordinated oxygen from the defect site, and lattice metal-oxygen, respectively (Fig. 2(g)) [8,56]. FESEM, Raman, XPS, TEM and EDS analyses confirmed that $CuCo_2O_4$ microflowers and NiO hexagonal nanosheets developed on the Ni foam surface in the CCO/NO electrode.

3.2. CV study of NO, CCO, and CCO/NO electrodes

Successfully prepared NO, CCO, and CCO/NO electrodes were evaluated as binder-free positive electrodes for a hybrid SC. CV of electrodes was performed in the positive potential windows from −0.1 V to 0.75 V. Prior to measurement the surface activation of electrodes was performed by CV to obtain stable performance [58]. Fig. 3(a) shows comparative CV profiles of Ni foam, NO, CCO, and CCO/NO electrodes at $\nu = 50$ mV s^{-1}. The CV profile shape showing broad oxidation and reduction peaks highlight the battery-like storage property of electrodes, typical for Ni-, Co-, and Cu-based nanostructured oxide materials in which kinetically faster redox reactions at the electrode surface generate most of the current due to better intercalation and diffusion of electrolyte ions [11,59]. Here CCO/NO exhibits a maximum enclosed area under the CV and higher currents at the redox peaks than NO and CCO. This could be associated with the presence of both $CuCo_2O_4$ and NiO together, generating more active sites for faradaic reactions. Its unique porous surface could enhance better electrolyte diffusion for faster redox reactions, boosting the overall electrochemical charge storage performance of CCO/NO [27,28,60,61]. The broad redox peak that appeared in the CV of NO is due to intercalation and interaction of OH^- from the electrolyte with NiO nanosheets, which could be presented by the following reaction [16,21].

$$nNiO + xOH^- \leftrightarrow xNiOOH + (n - x)NiO + ne^- \quad (14)$$

Similarly, for CCO, the broad redox peak appeared due to intercalation and interaction of OH^- from the electrolyte with $CuCo_2O_4$ nanosheet microflowers, presented by following reactions [62,63].

$$nCuCo_2O_4 + xH_2O + xe^- \leftrightarrow 2(n - x)CoOOH + (n - x)CuOH \quad (15)$$

$$CoOOH + OH^- \leftrightarrow CoO_2 + H_2O + e^- \quad (16)$$

$$CuOH + OH^- \leftrightarrow Cu(OH)_2 + e^- \quad (17)$$

Electrolyte interaction kinetics at the electrode surface can be studied using CV at different ν. In a further study, the CV of all electrodes was performed at different ν from 5 to 100 mV s^{-1}. Fig. 3(b) shows the CV profiles of CCO/NO at different ν. With an increasing ν, the enclosed area under CV and the redox peak current values increase, but the CV curve profile shape is maintained. This could be associated with faster redox charge transfer reactions at the electrode with increasing ν, depicting the remarkable charge transfer kinetics of CCO/NO. Furthermore, the observed electrochemical polarization at CV could be associated with increased internal diffusion resistance at the electrode due to faster redox transitions at higher ν, extending the separation between oxidation and reduction peaks [8,64]. Similar polarization behavior is observed for NO and CCO electrodes (Fig. S3). As the Ni-foam did not show any significant area under CV curve, its contribution into electrode charge storage was omitted.

At an applied ν, the $j(E)$ generated at the active CCO/NO surface can be the addition of surface current termed as capacitive current ($j_{cap} \propto \nu$) or diffusion-control current ($j_{diff} \propto \nu^{1/2}$). The inset of Fig. 3(b) shows the plot of j_{peak} vs $\nu^{1/2}$, where j_{peak} is the oxidation/reduction peak current density where most of the charge is generated (stored–retrieved). Linearity is observed between j_{peak} and $\nu^{1/2}$, indicating that the diffusion-controlled charge transfer reactions are evident at the porous

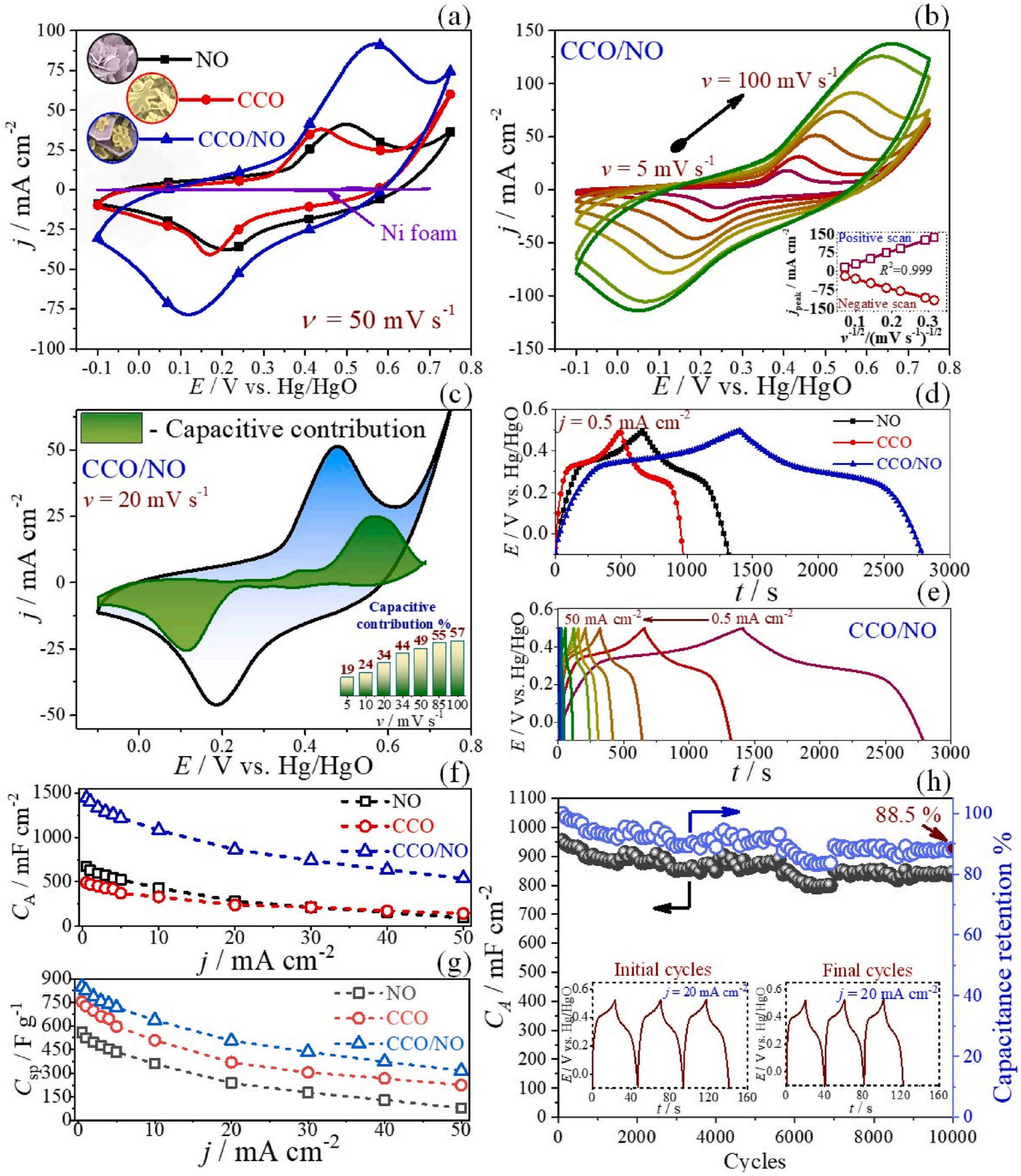

Fig. 3. (a) Cyclic voltammetry (CV) profiles of NO, CCO, and CCO/NO electrodes at $\nu = 50$ mV s^{-1}. (b) CV profiles of CCO/NO at various ν values [Inset: Plot of oxidation/reduction j_{peak} vs. $\nu^{1/2}$]. (c) CV profiles of CCO/NO at $\nu = 20$ mV s^{-1} and estimated capacitive contributing CV region [Inset: Plot of capacitive contribution percentage at different ν]. (d) Galvanostatic charge-discharge (GCD) profiles of NO, CCO, and CCO/NO electrodes at $j = 0.5$ mA cm^{-2}. (e) GCD profiles of CCO/NO at various j values. (f) Plot of C_A vs j for NO, CCO, and CCO/NO. (g) Plot of C_{sp} vs j for NO, CCO, and CCO/NO. (h) The C_A and capacitance retention plots for CCO/NO at different cycles [Inset: initial and final three consecutive GCD profiles recorded for 10,000 consecutive cycles].

CCO/NO structure, generating most of its current with remarkable reversibility [8]. The $j(E)$ at a given ν can be presented by the following relation.

$$j(E) = j_{\text{cap}}(E) + j_{\text{diff}}(E) = \mathrm{k}_1\, \nu + \mathrm{k}_2\, \nu^{1/2}, \tag{18}$$

Where k_1 and k_2 are proportionality constants. Using the reported method, quantitative estimation of the diffusion-controlled and capacitive contributions in the CV was estimated [4,8]. Fig. 3(c) shows the capacitive contribution of the CCO/NO electrode at $\nu = 20$ mV s^{-1}. Most of the capacitive current is generated at the potential region, except for broad oxidation and reduction peaks. At the peak regions, electrolyte ion intercalation could lead to faradaic transitions, generating diffusion-related currents. The inset of Fig. 3(c) shows that with the increasing ν, the capacitive current contributes more to the total current of CV, as electrolyte ions have less time to settle and intercalate at the electrode surface for diffusion-control interactions [8]. Similar behavior is observed for NO and CCO electrodes (Fig. S3 c, d). Fig. S4 shows a plot of estimated C_A from CV. At all ν, CCO/NO exhibits the maximum C_A, which can be ascribed to increased active sites and porous structure, leading to better conductivity and improved diffusion of electrolyte ions.

The CCO/NO exhibited a maximum C_A of 1074 mF cm^{-2} at $\nu = 5$ mV s^{-1}, far more than 562 mF cm^{-2} of NO and 378 mF cm^{-2} of CCO.

3.3. GCD study of NO, CCO, and CCO/NO electrodes

The GCD analysis of NO, CCO, and CCO/NO electrodes was performed between the potential from −0.1 to 0.5 V at different j from 0.5 mA cm^{-2} to 50 mA cm^{-2}. Fig. 3(d) shows comparative GCD profiles of electrodes at $j = 0.5$ mA cm^{-2}. All GCD shows nonlinear charging and discharging behavior. These GCD profiles show initial capacitive charging, rapidly increasing the electrode's potential, followed by a slow increase in potential due to electrolyte ion intercalation, facilitating redox reactions for diffusion-controlled charging. A similar process could be presented during discharging. However, these GCD profiles show symmetry across the charging and discharging process, indicating the high coulombic charge–discharge efficiency of electrodes [8]. In comparison, a CCO/NO exhibits a maximum charging-discharging time, supporting the CV studies. Fig. 3(e) shows the GCD profiles of the CCO/NO electrode at different j. Here, an increased charge transfer rate with an increased applied j effectively decreased the charge-discharge time [8]. Similar behavior is seen for NO and CCO (Fig. S5). The estimated C_A from GCD showed that the CCO/NO exhibited a maximum C_A of 1444 mF cm^{-2} ($C_{sp} = 849$ F g^{-1}/$Q = 409$ C g^{-1}), much higher than 672 mF cm^{-2} ($C_{sp} = 560$ F g^{-1}/$Q = 272$ C g^{-1}) of NO and 491 mF cm^{-2} ($C_{sp} = 755$ F g^{-1}/$Q = 368$ C g^{-1}) of CCO at $j = 0.5$ mA cm^{-2}. This maximum C_A by CCO/NO is more than some previous reports (Table S1). The improved areal capacitance of CCO/NO is associated with direct binder-free growth and the synergetic presence of NiO nanosheets and $CuCo_2O_4$ microstructures on a conducting Ni foam surface [27,28]. This superior charge storage performance by CCO/NO as the SC electrode and as active material is sustained at all j values (Fig. 3(f) and (g)). Stability studies of CCO/NO were conducted by continuous GCD cycling at $j = 20$ mA cm^{-2}. Fig. 3(h) shows the plot of C_A at 10,000 continuous cycles. After 10,000 cycles, 88.5% of initial capacitance was retained, illustrating its remarkable cyclic performance, higher than some previous reports [9,23,28,54,63,64]. After cleaning and vacuum drying of CCO/NO after 10,000 cycles, the recorded XRD (Fig. S6) did not show any significant change in the phase of materials supporting the stability results. Gradual increase in C_A after 1000 cycles could be associated with the activation of CCO/NO [33,54,65]. The inset of Fig. 3(h) shows the initial and final three continuous GCD profiles, showing the CCO/NO electrode's remarkably sustained coulombic charge-discharge efficiency.

3.4. EIS study of NO, CCO, and CCO/NO electrodes

The intrinsic impedance properties and surface electrochemical interactions can be studied using EIS analysis. For this, the NO, CCO, and CCO/NO electrodes were subjected to EIS analysis in the frequency (f) range of 0.01 Hz–0.1 M Hz. Fig. 4(a) shows the respective Nyquist plots of electrodes with real impedance (Z_{re}) on the X-axis and imaginary impedance (Z_{img}) on the Y-axis. These experimental EIS plots of all electrodes were further simulated with the equivalent circuit models (Fig. S7) [64–67]. Nyquist plots showed a pseudo-semicircle at the high-frequency region (inset of Fig. 4(a)) and a straight line at the low-frequency region. The intercept of the Nyquist plot on the Z_{re}-axis at the high-frequency end can be associated with electrolyte ohmic resistance and internal resistance of the electrode due to the electrode intrinsic resistance and contact resistance between the electrode material and current collector, termed as solution resistance (R_1). The pseudo-semicircle diameter observed in the high-frequency region represents the charge transfer resistance (R_2) that occurred during

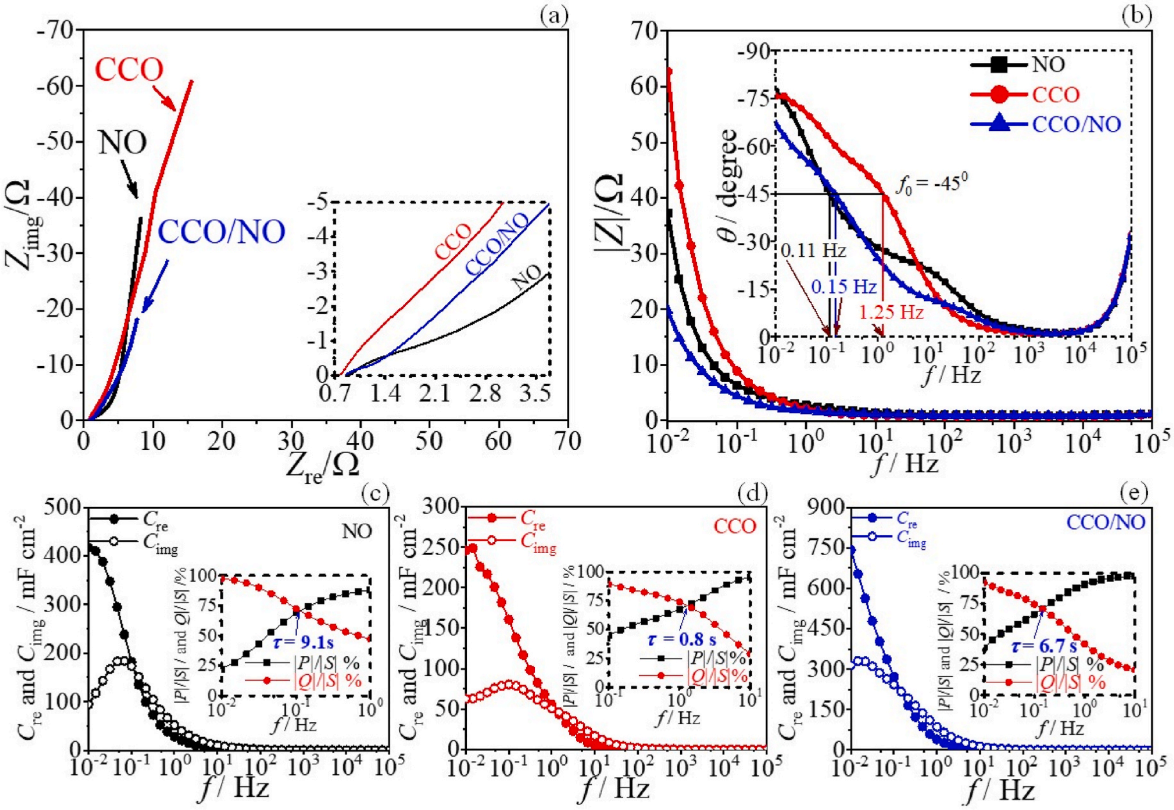

Fig. 4. (a) Nyquist plots of NO, CCO, and CCO/NO electrodes. [Inset: High-frequency region]. (b)Bode plots associated with Impedance (|Z|) vs frequency (f) of NO, CCO, and CCO/NO electrodes [Inset: Bode plots associate with Phase (θ) vs f of NO, CCO, and CCO/NO electrodes]. Frequency-dependent real (C_{re}) and imaginary (C_{img}) capacitance vs f plots of NO(c), CCO(d), and CCO/NO(e) [Inset: Plots of normalized active power $|P|/|S|$% and normalized reactive power $|Q|/|S|$% vs f].

electrolyte ion diffusion, followed by a redox reaction at the electrode's porous interface. In addition, the less oblique alignment of Nyquist plots to Z_{img}-axis at the low-frequency region indicates better ion diffusion at the electrode-electrolyte interface [68,69] R_1 values from equivalent circuit fitting for NO, CCO, and CCO/NO are 0.89 Ω, 0.77 Ω, and 0.83 Ω, respectively. Here, the lowered R_1 value of CCO/NO compared to NO indicated that $CuCo_2O_4$ microflowers on NiO nanosheets developed better electron conduction pathways, decreasing the electrode's overall solution resistance despite an increased active mass. Similarly, the CCO/NO showed the lowest R_2 value of 0.35 Ω compared to 3.68 Ω of NO and 3.79 Ω of CCO. This significantly reduced R_2 was due to the porous interface of CCO/NO shortening diffusion pathways for electrolyte ions, followed by effective charge transfer interactions justifying its high rate performance [36,66].

Fig. 4(b) shows Bode plots examining frequency-dependent impedance behavior of NO, CCO, and CCO/NO. The CCO/NO exhibited the lowest impedance at lower frequencies, supporting the Nyquist plots. Faster reaction kinetics response time ($\tau_0 = 1/f_0$) can be evaluated from the capacitive response frequency at the phase angle of $f_0 = -45^\circ$ from the bode plot of phase angle vs frequency (inset of Fig. 4(b)) [24,70,71]. CCO/NO exhibited τ_0 of 6.7 s smaller than 9.1 s of NO, indicating improved reaction kinetics on its interface. This τ_0 of 6.7 s is still lower

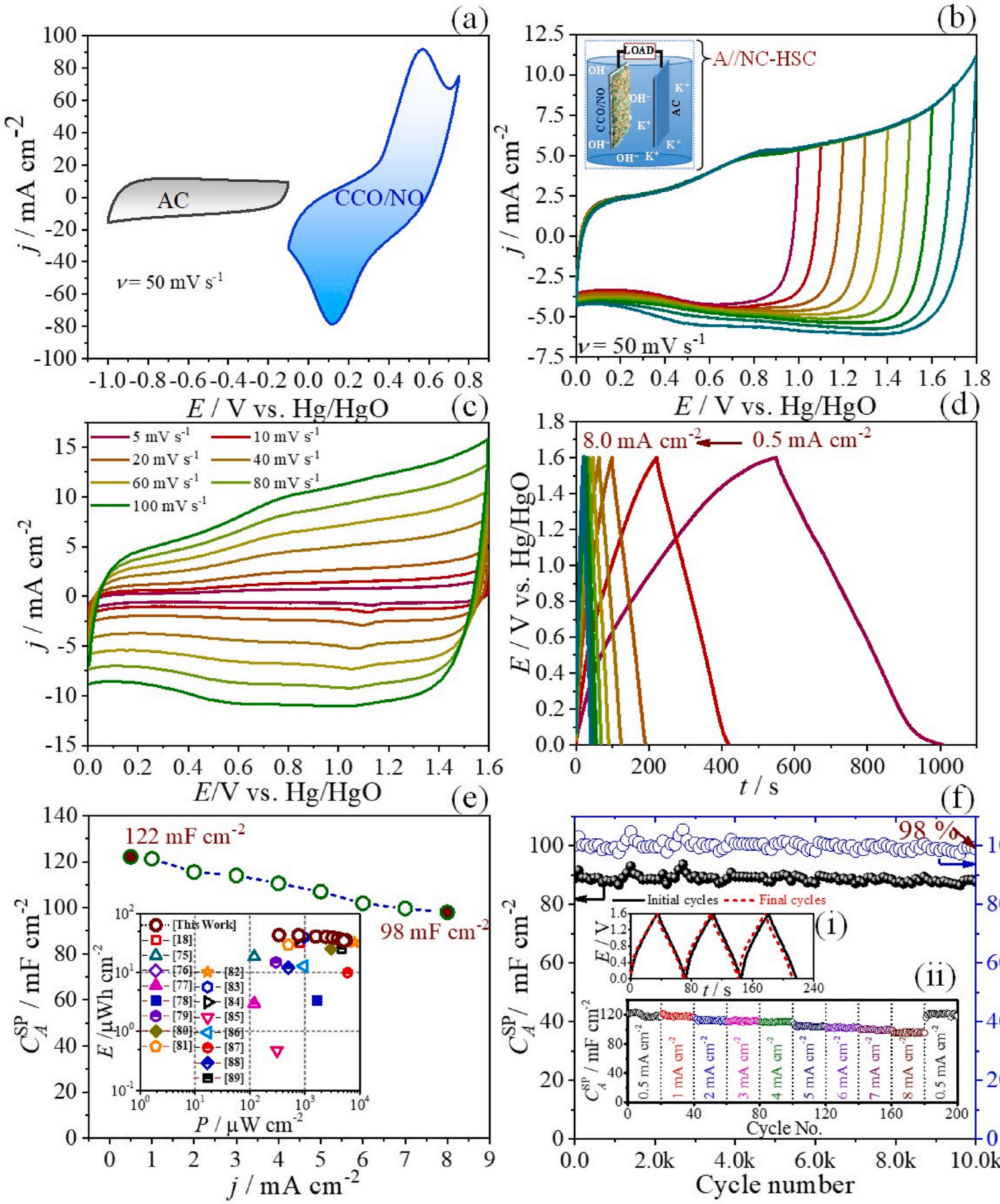

Fig. 5. (a) Cyclic voltammetry (CV) profiles of activated carbon (AC) and CCO/NO electrodes at $\nu = 50$ mV s^{-1}. (b) CV profiles with different potential windows of A//NC–HSC at $\nu = 50$ mV s^{-1}. (c) CV profiles of A//NC–HSC at various ν values. (d) GCD profiles of A//NC–HSC at various j values. (e) Plot of C_A^{SC} at different j values for A//NC–HSC [Inset: Ragone plot]. (f) Plot of C_A^{SC} and capacitance retention at different cycles [Inset: (i) Plot of initial and final three consecutive GCD profiles recorded for 10,000 consecutive cycles, (ii) Rate performance plot].

than physically prepared AC material ($\tau_0 = 12$ s) [72]. In ideal EDLC electrodes, the phase angle can be observed at $-90°$ at lower frequencies. Here, all electrodes exceed phase angles more than $-90°$ due to the resistive part associated with the faradaic transition and diffusion of ions [73]. In addition, frequency-dependent real capacitance (C_{re}) and imaginary capacitance (C_{img}) were estimated for NO (Fig. 4(c)), CCO (Fig. 4(d)), and CCO/NO (Fig. 4(e)) [8]. CCO/NO exhibits maximum C_{re} and C_{img} values, indicating higher capacitance performance supporting the CV and GCD studies [8].

Moreover, during the EIS operation of the equivalent circuit model, the power flow with the net transfer of energy can be termed real active power $P(\omega)$, and the power flow due to stored energy can be termed imaginary reactive power $Q(\omega)$. The total power flow can be expressed as complex power $S(\omega) = P(\omega) + jQ(\omega)$. An ideal capacitor has only reactive power contribution; however, pure resistance has only active power contribution during power flow. An equivalent circuit model can depict the electrode's behavior. The electrode behavior can switch between capacitive and resistive parts at different frequencies during EIS, similar to the simulated circuit. The plot of normalized real ($|P(\omega)|/|S(\omega)|$) and imaginary($|Q(\omega)|/|S(\omega)|$) parts of the complex power plot at different frequencies can be visualized as the electrode's switching behavior. Typically, at low frequencies, the capacitive behavior is dominant where no real power ($|P(\omega)|/|S(\omega)|$) is dissipated, whereas, at the high frequencies, the resistive behavior is dominant where most of the real power is dissipated [8,67]. These can be viewed as opposite trends in the normalized NO, CCO, and CCO/NO power plots (inset of Fig. 4(c–e)). At the resonating frequency (f_0), both plots crossover where the capacitive–resistive behavior can be equally contributing. The time constant estimated at f_0 corresponds to the phase angle $-45°$, representing the duration required to discharge its stored energy with an efficiency of more than 50% [8,67]. The obtained time constants for electrodes correlate well with Bode plots. The estimated time constant indicates that CCO exhibits more power performance than NO; however, the CCO/NO performance is in between.

3.5. *Performance study of hybrid SC*

An aqueous hybrid SC device was assembled in 2 M KOH using high-performance CCO/NO as a positive electrode and AC as a negative electrode [A//NC–HSC]. Fig. 5(a) shows combined CV profiles of AC and CCO/NO electrodes at $\nu = 50$ mV s^{-1}. AC shows rectangular CV behavior ascribed to EDLC charge storage behavior, and CCO/NO shows nonlinear faradic-dominated charge storage behavior [8]. Effectively, when both operated together in the A//NC–HSC (inset of Fig. 5(b)), it exhibited a pseudocapacitive behavior, as the CV curve's shape is near-rectangular (Fig. 5(b)). After running CV for various potential windows, 1.6 V was the best-suited potential for operating A//NC–HSC. The CV of A//NC–HSC was performed at ν values from 5 to 100 mV s^{-1} (Fig. 5(c)). Similar to single electrode CV behavior, the device showed an increase in anodic and cathodic currents, and maintained its symmetric and pseudocapacitive shape [23,25,74]. This shows excellent reversibility and a high-capacity A//NC–HSC performance. Similarly, Fig. 5(d) shows the GCD of A//NC–HSC at different j values from 0.5 to 8 mA cm^{-2}. It shows pseudocapacitive linear charge-discharge behavior, supporting the CV. Fig. 5(e) shows C_A^{SC} estimated from GCD curves at various j values. The A//NC–HSC exhibited a maximum C_A^{SC} of 122 mF cm^{-2} at j of 0.5 mA cm^{-2}. Fig. 5(e) shows the plot of C_A^{SC} at different applied j for A//NC–HSC. The E_A and P_A values were estimated at different j values. A//NC–HSC exhibited a maximum E_A of 43 μWh cm^{-2} at 0.5 mA cm^{-2} and a maximum P_A of 5.1 mW cm^{-2} at 8.0 mA cm^{-2}, outperforming previous reports [18,75–89]. The inset of Fig. 5(e) highlights the Ragone plot. The A//NC–HSC was evaluated for cyclic stability at $j = 4$ mA cm^{-2}. It showed outstanding capacity retention of 98% for 10,000 cycles (Fig. 5(f)), more than some previous reports [27,43,44,63,90]. The inset (i) of Fig. 5(f) shows the first and final three continuous GCD profiles of A//NC–HSC. It shows that the shape of GCD profiles was sustained, and the time for charging–discharging was maintained after 10,000 cycles, indicating outstanding performance and excellent coulombic efficiency of A//NC–HSC. The inset (ii) of Fig. 5(f) shows the plot of estimated C_A^{SC} at j from 0.5 mA cm^{-2} to 8 mA cm^{-2} for each 20 consecutive GCD cycles, showing the remarkable rate performance of A//NC–HSC. At each j, the device showed stable capacitance performance. The initial capacitance for $j = 0.5$ mA cm^{-2} GCD cycles is retained for final 20 GCD cycles. Self-discharge rates of individual electrodes CCO/NO (Fig. S8(b)) and AC (Fig. S8(c)) in A//NC–HSC (Fig. S8(a)) were measured for 18 h after charging the SC device for 1.6 V for 2 h. The prepared CCO/NO showed excellent discharge performance. During 18 h, the CCO/NO retained the stable OCP of 0.35 V *vs* Hg/HgO, highlighting the advantage of opted binder free method. However, AC carbon showed a sharp increase in the OCP, which stabilized at -0.02 V *vs* Hg/HgO. Preparation of AC using binders can cause an increase the internal resistance of the electrode, which could affect its discharge performance.

4. Conclusion

A simple, binder-free hydrothermal method was used for synthesizing a porous hybrid composite electrode comprising $CuCo_2O_4$ microflowers and NiO hexagonal nanosheets on conducting 3D Ni foam [CCO/NO]. For a comparative study, a similar method was applied for the synthesis of NiO hexagonal nanosheets on Ni foam [NO] and $CuCo_2O_4$ circular nanosheet microflowers on 3D Ni foam [CCO]. The electrochemical study revealed that hybrid composite CCO/NO in KOH showed enhanced capacitance performance as the positive electrode, compared to NO and CCO. This can be ascribed to hybrid nanocomposite synthesis, which provided extra redox-active sites for redox transitions, and the electrode's unique porous surface, which improved internal electrical conductivity and electrolyte ion diffusion. This unique hybrid composite CCO/NO exhibited a significantly high areal capacitance of 1444 mF cm^{-2} ($C_{sp} = 849$ F g^{-1}) compared to NO (672 mF cm^{-2}/$C_{sp} = 560$ F g^{-1}) and CCO (491 mF cm^{-2}/$C_{sp} = 755$ F g^{-1}), with excellent cyclic stability up to 88.5% for 10,000 GCD cycles. An aqueous hybrid SC A//NC–HSC was assembled with AC as a negative electrode, and CCO/NO as a positive in KOH showed an improved potential of 1.6 V and exhibited a maximum areal capacitance of 122 mF cm^{-2}, with a maximum areal energy density of 43 μWh cm^{-2} and a maximum areal power density of 5.1 mW cm^{-2}. Also, A//NC–HSC showed excellent cyclic stability up to 98% for 10,000 GCD cycles. This comparative study illustrated the significant enhancement of electrochemical properties of a stable, porous, hybrid composite electrode comprising $CuCo_2O_4$ and NiO than its parent oxide electrode useful for developing a cost-effective, high-performance electrode for hybrid supercapacitor application.

Declaration of competing interest

The authors declare that they have no known competing financial interests or personal relationships that could have appeared to influence the work reported in this paper.

Acknowledgements

This research was supported by the Basic Science Research Program through the National Research Foundation of Korea (NRF), funded by the Ministry of Education (NRF- 2018R1A6A1A03024962) and the Ministry of Science and ICT (NRF-2020R1A2C2100746).

Appendix A. Supplementary data

Supplementary data to this article can be found online at https://doi.org/10.1016/j.ceramint.2022.09.143.

References

[1] F. Li, L. Kong, Y. Sun, Y. Jin, P. Hou, Micron-sized monocrystalline $LiNi_{1/3}Co_{1/3}Mn_{1/3}O_2$ as high-volumetric-energy-density cathode for lithium-ion batteries, J. Mater. Chem. 6 (2018) 12344–12352, https://doi.org/10.1039/C8TA03363C.

[2] P. Hou, F. Li, Y. Sun, H. Li, X. Xu, T. Zhai, Multishell precursors facilitated synthesis of concentration-gradient nickel-rich cathodes for long-life and high-rate lithium-ion batteries, ACS Appl. Mater. Interfaces 10 (2018) 24508–24515, https://doi.org/10.1021/acsami.8b06286.

[3] S.K. Shinde, S.S. Karade, N.C. Maile, H.M. Yadav, G.S. Ghodake, A.D. Jagadale, D.-Y. Kim, Green synthesis of novel $CuCo_2O_4$ nanocomposite for stable hybrid supercapacitors by deep eutectic solvents, J. Mol. Liq. (2021), 116390, https://doi.org/10.1016/j.molliq.2021.116390.

[4] Y. Jiang, J. Liu, Definitions of pseudocapacitive materials: a brief review, ENERGY Environ. Mater. 2 (2019) 30–37, https://doi.org/10.1002/eem2.12028.

[5] M. Liu, Z. Cong, X. Pu, W. Guo, T. Liu, M. Li, Y. Zhang, W. Hu, Z.L. Wang, High-energy asymmetric supercapacitor yarns for self-charging power textiles, Adv. Funct. Mater. 29 (2019), 1806298, https://doi.org/10.1002/adfm.201806298.

[6] P. Simon, Y. Gogotsi, Perspectives for electrochemical capacitors and related devices, Nat. Mater. 19 (2020) 1151–1163, https://doi.org/10.1038/s41563-020-0747-z.

[7] D.P. Dubal, O. Ayyad, V. Ruiz, P. Gómez-Romero, Hybrid energy storage: the merging of battery and supercapacitor chemistries, Chem. Soc. Rev. 44 (2015) 1777–1790, https://doi.org/10.1039/C4CS00266K.

[8] N.C. Maile, M. Moztahida, A.A. Ghani, M. Hussain, K. Tahir, B. Kim, S.K. Shinde, V. J. Fulari, D.S. Lee, Electrochemical synthesis of binder-free interconnected nanosheets of Mn-doped Co_3O_4 on Ni foam for high-performance electrochemical energy storage application, Chem. Eng. J. 421 (2021), 129767, https://doi.org/10.1016/j.cej.2021.129767.

[9] Y. Wang, D. Yang, J. Lian, J. Pan, T. Wei, Y. Sun, Cedar leaf-like $CuCo_2O_4$ directly grow on nickel foam by a hydrothermal/annealing process as an electrode for a high-performance symmetric supercapacitor, J. Alloys Compd. 735 (2018) 2046–2052, https://doi.org/10.1016/j.jallcom.2017.12.005.

[10] D.P. Dubal, N.R. Chodankar, R. Holze, D.-H. Kim, P. Gomez-Romero, Ultrathin mesoporous $RuCo_2O_4$ nanoflakes: an advanced electrode for high-performance asymmetric supercapacitors, ChemSusChem 10 (2017) 1771–1782, https://doi.org/10.1002/cssc.201700001.

[11] N.R. Chodankar, H.D. Pham, A.K. Nanjundan, J.F.S. Fernando, K. Jayaramulu, D. Golberg, Y. Han, D.P. Dubal, True meaning of pseudocapacitors and their performance metrics: asymmetric versus hybrid supercapacitors, Small 16 (2020), 2002806, https://doi.org/10.1002/smll.202002806.

[12] L. Hao, X. Li, L. Zhi, Carbonaceous electrode materials for supercapacitors, Adv. Mater. 25 (2013) 3899–3904, https://doi.org/10.1002/adma.201301204.

[13] Y.J. Gu, W. Wen, S. Zheng, J.M. Wu, Monocrystalline $FeMnO_3$ on carbon cloth for extremely high-areal-capacitance supercapacitors, ACS Appl. Energy Mater. 3 (2020) 11863–11872, https://doi.org/10.1021/acsaem.0c01996.

[14] F. Yu, T. Huang, P. Zhang, Y. Tao, F.Z. Cui, Q. Xie, S. Yao, F. Wang, Design and synthesis of electrode materials with both battery-type and capacitive charge storage, Energy Storage Mater. 22 (2019) 235–255, https://doi.org/10.1016/j.ensm.2019.07.023.

[15] J. Liu, J. Wang, C. Xu, H. Jiang, C. Li, L. Zhang, J. Lin, Z.X. Shen, Advanced energy storage devices: basic principles, analytical methods, and rational materials design, Adv. Sci. 5 (2018), https://doi.org/10.1002/advs.201700322.

[16] J. Zhao, Y. Tian, A. Liu, L. Song, Z. Zhao, The NiO electrode materials in electrochemical capacitor: a review, Mater. Sci. Semicond. Process. 96 (2019) 78–90, https://doi.org/10.1016/j.mssp.2019.02.024.

[17] Y. Fan, Z. Ma, L. Wang, Y. Dong, T. Jiang, Z. Li, L. Liu, G. Shao, In-situ synthesis of NiO foamed sheets on Ni foam as efficient cathode of battery-type supercapacitor, Electrochim. Acta 269 (2018) 62–69, https://doi.org/10.1016/j.electacta.2018.02.141.

[18] L. Wang, M. Huang, S. Chen, L. Kang, X. He, Z. Lei, F. Shi, H. Xu, Z.-H. Liu, δ-MnO_2 nanofiber/single-walled carbon nanotube hybrid film for all-solid-state flexible supercapacitors with high performance, J. Mater. Chem. A. 5 (2017) 19107–19115, https://doi.org/10.1039/C7TA04712F.

[19] J.H. Kwak, Y.-W. Lee, J.H. Bang, Supercapacitor electrode with an ultrahigh Co_3O_4 loading for a high areal capacitance, Mater. Lett. 110 (2013) 237–240, https://doi.org/10.1016/j.matlet.2013.08.032.

[20] K. Xiao, J.-W. Li, G.-F. Chen, Z.-Q. Liu, N. Li, Y.-Z. Su, Amorphous MnO_2 supported on 3D-Ni nanodendrites for large areal capacitance supercapacitors, Electrochim. Acta 149 (2014) 341–348, https://doi.org/10.1016/j.electacta.2014.10.117.

[21] Y. Chen, Y. Wang, P. Sun, P. Yang, L. Du, W. Mai, Nickel oxide nanoflake-based bifunctional glass electrodes with superior cyclic stability for energy storage and electrochromic applications, J. Mater. Chem. A. 3 (2015) 20614–20618, https://doi.org/10.1039/C5TA04011F.

[22] H. Zhang, D. Xiao, Q. Li, Y. Ma, S. Yuan, L. Xie, C. Chen, C. Lu, Porous $NiCo_2O_4$ nanowires supported on carbon cloth for flexible asymmetric supercapacitor with high energy density, J. Energy Chem. 27 (2018) 195–202, https://doi.org/10.1016/j.jechem.2017.10.034.

[23] Y. Feng, W. Liu, Y. Wang, W. Gao, J. Li, K. Liu, X. Wang, J. Jiang, Oxygen vacancies enhance supercapacitive performance of $CuCo_2O_4$ in high-energy-density asymmetric supercapacitors, J. Power Sources 458 (2020), 228005, https://doi.org/10.1016/j.jpowsour.2020.228005.

[24] L. Kumar, H. Chauhan, N. Yadav, N. Yadav, S.A. Hashmi, S. Deka, Faster ion switching $NiCo_2O_4$ nanoparticle electrode-based supercapacitor device with high performances and long cycling stability, ACS Appl. Energy Mater. 1 (2018) 6999–7006, https://doi.org/10.1021/acsaem.8b01427.

[25] J. Chen, H. Zhang, H. Wang, Y. Lin, Y. Tang, H. Shao, S. Zhang, Design and construction of hollow nanocube $NiMoO_4$ electrode with high performance for asymmetric supercapacitor, J. Nanostructure Chem. (2022), https://doi.org/10.1007/s40097-021-00458-x.

[26] Q. Wang, D. Chen, D. Zhang, Electrospun porous $CuCo_2O_4$ nanowire network electrode for asymmetric supercapacitors, RSC Adv. 5 (2015) 96448–96454, https://doi.org/10.1039/C5RA21170K.

[27] D. Yao, Y. Ouyang, X. Jiao, H. Ye, W. Lei, X. Xia, L. Lu, Q. Hao, Hierarchical NiO@$NiCo_2O_4$ core-shell nanosheet arrays on Ni foam for high-performance electrochemical supercapacitors, Ind. Eng. Chem. Res. 57 (2018) 6246–6256, https://doi.org/10.1021/acs.iecr.8b00467.

[28] G. Zhang, T. Wang, X. Yu, H. Zhang, H. Duan, B. Lu, Nanoforest of hierarchical Co_3O_4@$NiCo_2O_4$ nanowire arrays for high-performance supercapacitors, Nano Energy 2 (2013) 586–594, https://doi.org/10.1016/j.nanoen.2013.07.008.

[29] K. Xu, X. Yang, J. Yang, J. Hu, Synthesis of hierarchical Co_3O_4@$NiCo_2O_4$ core-shell nanosheets as electrode materials for supercapacitor application, J. Alloys Compd. 700 (2017) 247–251, https://doi.org/10.1016/j.jallcom.2017.01.071.

[30] Q. Wang, J. Xu, X. Wang, B. Liu, X. Hou, G. Yu, P. Wang, D. Chen, G. Shen, Core-shell CuCo2O4@MnO2 nanowires on carbon fabrics as high-performance materials for flexible, all-solid-state, electrochemical capacitors, Chemelectrochem 1 (2014) 559–564, https://doi.org/10.1002/celc.201300084.

[31] K. Qiu, M. Lu, Y. Luo, X. Du, Engineering hierarchical nanotrees with CuCo 2 O 4 trunks and NiO branches for high-performance supercapacitors, J. Mater. Chem. A. 5 (2017) 5820–5828, https://doi.org/10.1039/C7TA00506G.

[32] F. Li, M. Huang, J. Wang, J. Qu, Y. Li, L. Liu, V.K. Bandari, Y. Hong, B. Sun, M. Zhu, F. Zhu, Y.X. Zhang, O.G. Schmidt, On-chip 3D interdigital micro-supercapacitors with ultrahigh areal energy density, Energy Storage Mater. 27 (2020) 17–24, https://doi.org/10.1016/j.ensm.2020.01.008.

[33] M. Pang, S. Jiang, J. Zhao, S. Zhang, R. Liu, W. Qu, Q. Pan, B. Xing, L. Gu, H. Wang, Designed fabrication of three-dimensional δ-MnO 2 -cladded CuCo 2 O 4 composites as an outstanding supercapacitor electrode material, New J. Chem. 42 (2018) 19153–19163, https://doi.org/10.1039/C8NJ03774D.

[34] Y. Zhao, Effect of precursor on the morphology and supercapacitor performance of CuCo2O4, Int. J. Electrochem. Sci. 14 (2019) 3885–3896, https://doi.org/10.20964/2019.04.62.

[35] K. Song, W. Ai, Y. Zhang, Y. Zeng, Y. Yu, H. Qiao, Z. Liu, X. Shen, X. Hu, X. Hu, Three-dimensional self-supported CuCo2O4nanowires@NiO nanosheets core/shell arrays as an oxygen electrode catalyst for Li-O2batteries, J. Mater. Chem. A. 9 (2021) 3007–3017, https://doi.org/10.1039/d0ta09195b.

[36] H. Wang, Y. Li, D. Deng, M. Li, C. Zhang, L. Luo, NiO-coated CuCo 2 O 4 nanoneedle arrays on carbon cloth for non-enzymatic glucose sensing, ACS Appl. Nano Mater. 4 (2021) 9821–9830, https://doi.org/10.1021/acsanm.1c02228.

[37] K. Xu, S. Ma, Y. Shen, Q. Ren, J. Yang, X. Chen, J. Hu, CuCo2O4 nanowire arrays wrapped in metal oxide nanosheets as hierarchical multicomponent electrodes for supercapacitors, Chem. Eng. J. 369 (2019) 363–369, https://doi.org/10.1016/j.cej.2019.03.079.

[38] K. Malaie, M.R. Ganjali, T. Alizadeh, P. Norouzi, Simple electrochemical preparation of nanoflake-like copper oxide on Cu-plated nickel foam for supercapacitor electrodes with high areal capacitance, J. Mater. Sci. Mater. Electron. 28 (2017) 14631–14637, https://doi.org/10.1007/s10854-017-7327-2.

[39] Y. Qiu, Y. Zhao, X. Yang, W. Li, Z. Wei, J. Xiao, S.-F. Leung, Q. Lin, H. Wu, Y. Zhang, Z. Fan, S. Yang, Three-dimensional metal/oxide nanocone arrays for high-performance electrochemical pseudocapacitors, Nanoscale 6 (2014) 3626–3631, https://doi.org/10.1039/C3NR06675D.

[40] Z. Bi, X. Li, Y. Chen, X. Xu, S. Zhang, Q. Zhu, Bi-functional flexible electrodes based on tungsten trioxide/zinc oxide nanocomposites for electrochromic and energy storage applications, Electrochim. Acta 227 (2017) 61–68, https://doi.org/10.1016/j.electacta.2017.01.003.

[41] L. Li, J. Xu, J. Lei, J. Zhang, F. McLarnon, Z. Wei, N. Li, F. Pan, A one-step, cost-effective green method to in situ fabricate $Ni(OH)_2$ hexagonal platelets on Ni foam as binder-free supercapacitor electrode materials, J. Mater. Chem. A. 3 (2015) 1953–1960, https://doi.org/10.1039/C4TA05156D.

[42] R. Venkatkarthick, J. Qin, A new 3D composite of V_2O_5-based biodegradable ceramic material prepared by an environmentally friendly thermal method for supercapacitor applications, Environ. Technol. Innovat. 22 (2021), 101474, https://doi.org/10.1016/j.eti.2021.101474.

[43] K. Zhao, H. Wang, C. Zhu, S. Lin, Z. Xu, X. Zhang, Free-standing MXene film modified by amorphous FeOOH quantum dots for high-performance asymmetric supercapacitor, Electrochim. Acta 308 (2019) 1–8, https://doi.org/10.1016/j.electacta.2019.03.225.

[44] L. Zhi, W. Zhang, L. Dang, J. Sun, F. Shi, H. Xu, Z. Liu, Z. Lei, Holey nickel-cobalt layered double hydroxide thin sheets with ultrahigh areal capacitance, J. Power Sources 387 (2018) 108–116, https://doi.org/10.1016/j.jpowsour.2018.03.063.

[45] P. Zhang, Y. Li, G. Wang, F. Wang, S. Yang, F. Zhu, X. Zhuang, O.G. Schmidt, X. Feng, Zn-Ion hybrid micro-supercapacitors with ultrahigh areal energy density and long-term durability, Adv. Mater. 31 (2019), 1806005, https://doi.org/10.1002/adma.201806005.

[46] N.C. Maile, A.A. Ghani, S.K. Shinde, B. Kim, Y. Lim, K. Tahir, K.C. Devarayapalli, S. V. Mohite, J. Jang, D.S. Lee, Electrochemical studies of $Ni(OH)_2$, NiO, and Ni_3S_2 nanostructures on Ni-foam toward binder-free positive electrode for hybrid supercapacitor application, Int. J. Energy Res. (2022), https://doi.org/10.1002/er.8553.

[47] R.S. Feigelson, 50 Years of progress in crystal growth, J. Cryst. Growth 264 (2004), https://doi.org/10.1016/j.jcrysgro.2004.01.042 xi–xvi.

[48] R.B. Waghmode, N.C. Maile, D.S. Lee, A.P. Torane, Chemical bath synthesis of $NiCo_2O_4$ nanoflowers with nanorods like thin film for flexible supercapacitor

application-effect of urea concentration on structural conversion, Electrochim. Acta 350 (2020), 136413, https://doi.org/10.1016/j.electacta.2020.136413.

[49] Q. Gao, J. Wang, J. Wang, Morphology-controllable synthesis of CuCo$_2$O$_4$ arrays on Ni foam as advanced electrodes for supercapacitors, J. Alloys Compd. 789 (2019) 193–200, https://doi.org/10.1016/j.jallcom.2019.03.041.

[50] J.-F. Gao, J.-F. Hou, L.-B. Kong, Solid-state phase transformation of NiO into metallic Ni via ammonia reduction reaction for hybrid supercapacitors, Synth. Met. 281 (2021), 116899, https://doi.org/10.1016/j.synthmet.2021.116899.

[51] Z. Wang, Q. Shen, J. Xue, R. Guan, Q. Li, X. Liu, H. Jia, Y. Wu, 3D hierarchically porous NiO/NF electrode for the removal of chromium(VI) from wastewater by electrocoagulation, Chem. Eng. J. 402 (2020), 126151, https://doi.org/10.1016/j.cej.2020.126151.

[52] M. Qin, H. Liang, X. Zhao, H. Wu, Filter paper templated one-dimensional NiO/NiCo$_2$O$_4$ microrod with wideband electromagnetic wave absorption capacity, J. Colloid Interface Sci. 566 (2020) 347–356, https://doi.org/10.1016/j.jcis.2020.01.114.

[53] C. Chang, L. Zhang, C.-W. Hsu, X.-F. Chuah, S.-Y. Lu, Mixed NiO/NiCo$_2$O$_4$ nanocrystals grown from the skeleton of a 3D porous nickel network as efficient electrocatalysts for oxygen evolution reactions, ACS Appl. Mater. Interfaces 10 (2018) 417–426, https://doi.org/10.1021/acsami.7b13127.

[54] A.K. Das, N.H. Kim, S.H. Lee, Y. Sohn, J.H. Lee, Facile synthesis of CuCo$_2$O$_4$ composite octahedrons for high performance supercapacitor application, Compos. B Eng. 150 (2018) 269–276, https://doi.org/10.1016/j.compositesb.2018.07.021.

[55] A.Y. Faid, A.O. Barnett, F. Seland, S. Sunde, Ni/NiO nanosheets for alkaline hydrogen evolution reaction: in situ electrochemical-Raman study, Electrochim. Acta 361 (2020), 137040, https://doi.org/10.1016/j.electacta.2020.137040.

[56] X. Du, X. Zhang, Z. Xu, Z. Yang, Y. Gong, CuCo$_2$O$_4$ microflowers catalyst with oxygen evolution activity comparable to that of noble metal, Int. J. Hydrogen Energy 43 (2018) 5012–5018, https://doi.org/10.1016/j.ijhydene.2018.01.142.

[57] R. Sakthivel, J.-H. He, R.-J. Chung, Self-templating hydrothermal synthesis of carbon-confined double-shelled Ni/NiO hollow microspheres for diphenylamine detection in fruit samples, J. Hazard Mater. 424 (2022), 127378, https://doi.org/10.1016/j.jhazmat.2021.127378.

[58] T. Wang, Y. Wang, J. Lei, K. Chen, H. Wang, Electrochemically induced surface reconstruction of Ni-Co oxide nanosheet arrays for hybrid supercapacitors, Explorations 1 (2021), 20210178, https://doi.org/10.1002/EXP.20210178.

[59] Y. Tang, W. Guo, R. Zou, Nickel-based bimetallic battery-type materials for asymmetric supercapacitors, Coord. Chem. Rev. 451 (2022), 214242, https://doi.org/10.1016/j.ccr.2021.214242.

[60] X.M. Cao, Z.B. Han, Hollow core-shell ZnO@ZIF-8 on carbon cloth for flexible supercapacitors with ultrahigh areal capacitance, Chem. Commun. 55 (2019) 1746–1749, https://doi.org/10.1039/c8cc09847f.

[61] P. Song, X. He, M. Xie, J. Tao, X. Shen, Z. Ji, Z. Yan, L. Zhai, A. Yuan, Polyaniline wrapped graphene functionalized textile with ultrahigh areal capacitance and energy density for high-performance all-solid-state supercapacitors for wearable electronics, Compos. Sci. Technol. 198 (2020), 108305, https://doi.org/10.1016/j.compscitech.2020.108305.

[62] L. Liao, H. Zhang, W. Li, X. Huang, Z. Xiao, K. Xu, J. Yang, R. Zou, J. Hu, Facile synthesis of maguey-like CuCo$_2$O$_4$ nanowires with high areal capacitance for supercapacitors, J. Alloys Compd. 695 (2017) 3503–3510, https://doi.org/10.1016/j.jallcom.2016.12.004.

[63] W. Liu, Y. Feng, L. Sun, Y. Zhang, G. Wang, L. Zhao, M. Meng, J. Li, K. Liu, Hierarchical CuCo$_2$O$_4$ nanourchin supported by Ni foam with superior electrochemical performance, J. Alloys Compd. 756 (2018) 68–75, https://doi.org/10.1016/j.jallcom.2018.05.026.

[64] X. Ren, C. Guo, L. Xu, T. Li, L. Hou, Y. Wei, Facile synthesis of hierarchical mesoporous honeycomb-like NiO for aqueous asymmetric supercapacitors, ACS Appl. Mater. Interfaces 7 (2015) 19930–19940, https://doi.org/10.1021/acsami.5b04094.

[65] K. Xu, S. Ma, Y. Shen, Q. Ren, J. Yang, X. Chen, J. Hu, CuCo$_2$O$_4$ nanowire arrays wrapped in metal oxide nanosheets as hierarchical multicomponent electrodes for supercapacitors, Chem. Eng. J. 369 (2019) 363–369, https://doi.org/10.1016/j.cej.2019.03.079.

[66] M. Fan, B. Ren, L. Yu, D. Song, Q. Liu, J. Liu, J. Wang, X. Jing, L. Liu, Facile synthesis of Co3O4 nanowires grown on hollow NiO microspheres with superior electrochemical performance, Electrochim. Acta 166 (2015) 168–173, https://doi.org/10.1016/j.electacta.2015.03.090.

[67] H. Randriamahazaka, K. Asaka, Electromechanical analysis by means of complex capacitance of bucky-gel actuators based on single-walled carbon nanotubes and an ionic liquid, J. Phys. Chem. C 114 (2010) 17982–17988, https://doi.org/10.1021/jp106232s.

[68] Y. Xu, X. Huang, Z. Lin, X. Zhong, Y. Huang, X. Duan, One-step strategy to graphene/Ni(OH)$_2$ composite hydrogels as advanced three-dimensional supercapacitor electrode materials, Nano Res. 6 (2013) 65–76, https://doi.org/10.1007/s12274-012-0284-4.

[69] C. Zhang, Q. Chen, H. Zhan, Supercapacitors based on reduced graphene oxide nanofibers supported Ni(OH)$_2$ nanoplates with enhanced electrochemical performance, ACS Appl. Mater. Interfaces 8 (2016) 22977–22987, https://doi.org/10.1021/acsami.6b05255.

[70] A.K. Singh, D. Sarkar, K. Karmakar, K. Mandal, G.G. Khan, High-performance supercapacitor electrode based on cobalt oxide-manganese dioxide-nickel oxide ternary 1D hybrid nanotubes, ACS Appl. Mater. Interfaces 8 (2016) 20786–20792, https://doi.org/10.1021/acsami.6b05933.

[71] A. Gupta, S. Sardana, J. Dalal, S. Lather, A.S. Maan, R. Tripathi, R. Punia, K. Singh, A. Ohlan, Nanostructured polyaniline/graphene/Fe$_2$O$_3$ composites hydrogel as a high-performance flexible supercapacitor electrode material, ACS Appl. Energy Mater. 3 (2020) 6434–6446, https://doi.org/10.1021/acsaem.0c00684.

[72] A. Adan-Mas, L. Alcaraz, P. Arévalo-Cid, F.A. López-Gómez, F. Montemor, Coffee-derived activated carbon from second biowaste for supercapacitor applications, Waste Manag. 120 (2021) 280–289, https://doi.org/10.1016/j.wasman.2020.11.043.

[73] M. Zhu, L. Yu, S. He, H. Hong, J. Liu, L. Gan, M. Long, Highly efficient and stable cellulose-based ion gel polymer electrolyte for solid-state supercapacitors, ACS Appl. Energy Mater. 2 (2019) 5992–6001, https://doi.org/10.1021/acsaem.9b01109.

[74] Y.X. Zeng, Y. Han, Y.T. Zhao, Y. Zeng, M.H. Yu, Y.J. Liu, H.L. Tang, Y.X. Tong, X. H. Lu, Advanced Ti-doped Fe$_2$O$_3$@PEDOT core/shell anode for high-energy asymmetric supercapacitors, Adv. Energy Mater. 5 (2015), 1402176, https://doi.org/10.1002/aenm.201402176.

[75] F. Chen, Y. Ji, Y. Deng, F. Ren, S. Tan, Z. Wang, Ultrasonic-assisted fabrication of porous carbon materials derived from agricultural waste for solid-state supercapacitors, J. Mater. Sci. 55 (2020) 11512–11523, https://doi.org/10.1007/s10853-020-04751-y.

[76] H. Tang, Y. Yuan, L. Meng, W. Wang, J. Lu, Y. Zeng, T. Huang, C. Gao, Low-resistance porous nanocellular MnSe electrodes for high-performance all-solid-state battery-supercapacitor hybrid devices, Adv. Mater. Technol. 3 (2018), 1800074, https://doi.org/10.1002/admt.201800074.

[77] S. Surendran, R.K. Selvan, Growth and characterization of 3D flower-like β-NiS on carbon cloth: a dexterous and flexible multifunctional electrode for supercapattery and water-splitting applications, Adv. Mater. Interfac. 5 (2018) 1–12, https://doi.org/10.1002/admi.201701056.

[78] M. Karuppaiah, P. Sakthivel, S. Asaithambi, V. Balaji, G. Vijayaprasath, R. Yuvakkumar, G. Ravi, In-situ deposition of amorphous Tungsten(VI) oxide thin-film for solid-state symmetric supercapacitor, Ceram. Int. 48 (2022) 2510–2521, https://doi.org/10.1016/j.ceramint.2021.10.033.

[79] H. Zhou, G. Han, Y. Xiao, Y. Chang, H.-J. Zhai, Facile preparation of polypyrrole/graphene oxide nanocomposites with large areal capacitance using electrochemical codeposition for supercapacitors, J. Power Sources 263 (2014) 259–267, https://doi.org/10.1016/j.jpowsour.2014.04.039.

[80] Z. Tang, C. Jia, Z. Wan, Q. Zhou, X. Ye, Y. Zhu, Facile preparation of CoNi$_2$S$_4$@NiSe nano arrays on compressed nickel foam for high performance flexible supercapacitors, RSC Adv. 6 (2016) 112307–112316, https://doi.org/10.1039/C6RA20871A.

[81] M. Ojha, M. Deepa, Molybdenum selenide nanotubes decorated carbon net for a high performance supercapacitor, Chem. Eng. J. 368 (2019) 772–783, https://doi.org/10.1016/j.cej.2019.03.002.

[82] C. Shi, J. Sun, Y. Pang, Y. Liu, B. Huang, B.-T. Liu, A new potassium dual-ion hybrid supercapacitor based on battery-type Ni(OH)2 nanotube arrays and pseudocapacitor-type V2O5-anchored carbon nanotubes electrodes, J. Colloid Interface Sci. 607 (2022) 462–469, https://doi.org/10.1016/j.jcis.2021.09.011.

[83] N. Wang, X. Wang, Y. Zhang, W. Hou, Y. Chang, H. Song, Y. Zhao, G. Han, All-in-one flexible asymmetric supercapacitor based on composite of polypyrrole-graphene oxide and poly(3,4-ethylenedioxythiophene), J. Alloys Compd. 835 (2020), 155299, https://doi.org/10.1016/j.jallcom.2020.155299.

[84] B.K. Singh, A. Shaikh, R.O. Dusane, S. Parida, Copper oxide nanosheets and nanowires grown by one-step linear sweep voltammetry for supercapacitor application, J. Energy Storage 31 (2020), 101631, https://doi.org/10.1016/j.est.2020.101631.

[85] S. Tan, K.D. Li-Oakey, Effect of structural orientation on the performance of supercapacitor electrodes from electrospun coal-derived carbon nanofibers (CCNFs), J. Electrochem. Soc. 166 (2019) A3294–A3304, https://doi.org/10.1149/2.0651914jes.

[86] Y. Li, H. Jiang, X. Yan, Y. Zhu, W. Zhang, M. Zhang, W. Zhu, M.S. Javed, J. Pan, S. Hussain, 3D nanostructured Cu$_x$O modified copper foam as a binder-free electrode for all-solid-state supercapacitor, Ceram. Int. 47 (2021) 31138–31148, https://doi.org/10.1016/j.ceramint.2021.07.288.

[87] P.P. Ma, Q.L. Lu, N. Lei, Y.K. Liu, B. Yu, J.M. Dai, S.H. Li, G.H. Jiang, Effect of A-site substitution by Ca or Sr on the structure and electrochemical performance of LaMnO$_3$ perovskite, Electrochim. Acta 332 (2020), 135489, https://doi.org/10.1016/j.electacta.2019.135489.

[88] S.-H. Chou, L.-Y. Lin, Y.-H. Chiu, Pulse reverse electrodeposited nickel cobalt sulfide nanosheets on Ni foam as battery-type electrode for battery supercapacitor hybrids, J. Energy Storage 25 (2019), 100903, https://doi.org/10.1016/j.est.2019.100903.

[89] J. Chen, Y. Ren, H. Zhang, F. Zhou, J. Qi, Y. Sui, F. Wei, Self-supporting in situ growth Ni$_3$S$_2$/FL-Ti$_3$C$_2$ (MXene)/Ni composite as positive electrode for asymmetrical supercapacitor, J. Mater. Sci. Mater. Electron. 32 (2021) 9721–9729, https://doi.org/10.1007/s10854-021-05633-y.

[90] S.K. Shinde, S.S. Karade, H.M. Yadav, N.C. Maile, G.S. Ghodake, A.D. Jagadale, M. B. Jalak, N. Velhal, R. Kumar, D.S. Lee, D.-Y. Kim, Deep eutectic solvent mediated nanostructured copper oxide as a positive electrode material for hybrid supercapacitor device, J. Mol. Liq. 341 (2021), 117319, https://doi.org/10.1016/j.molliq.2021.117319.